Journal of Colloid and Interface Science 660 (2024) 66–76

Contents lists available at ScienceDirect

Journal of Colloid And Interface Science

journal homepage: www.elsevier.com/locate/jcis

Regular Article

Evolution of the structure of lipid nanoparticles for nucleic acid delivery: From *in situ* studies of formulation to colloidal stability

Jennifer Gilbert [a,b], Federica Sebastiani [a,c], Marianna Yanez Arteta [d], Ann Terry [e], Anna Fornell [e], Robert Russell [f], Najet Mahmoudi [g], Tommy Nylander [a,b,h,i,*]

[a] *Division of Physical Chemistry, Department of Chemistry, Lund University, 221 00 Lund, Sweden*
[b] *NanoLund, Lund University, Professorsgatan 1, 223 63 Lund, Sweden*
[c] *Department of Pharmacy, University of Copenhagen, Universitetsparken 2, 2100 København Ø, Denmark*
[d] *Advanced Drug Delivery, Pharmaceutical Sciences, R&D, AstraZeneca, 431 83, Gothenburg, Sweden*
[e] *MAX IV Laboratory, Lund University, Fotongatan 2, 224 84 Lund, Sweden*
[f] *National Deuteration Facility (NDF), Australian Nuclear Science and Technology Organisation (ANSTO), Lucas Heights, 2232 Sydney, NSW, Australia*
[g] *ISIS Neutron and Muon Source, Harwell Science and Innovation Campus, Didcot OX11 0QX, UK*
[h] *LINXS Institute of Advanced Neutron and X-Ray Science, Lund, Sweden*
[i] *School of Chemical Engineering and Translational Nanobioscience Research Center, Sungkyunkwan University, Suwon, Republic of Korea*

GRAPHICAL ABSTRACT

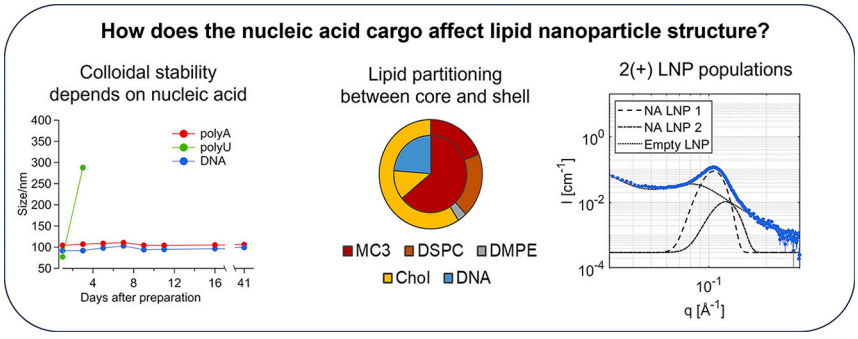

ABSTRACT

The development of lipid nanoparticle (LNP) based therapeutics for delivery of RNA has triggered the advance of new strategies for formulation, such as high throughput microfluidics for precise mixing of components into well-defined particles. In this study, we have characterised the structure of LNPs throughout the formulation process using *in situ* small angle x-ray scattering in the microfluidic chip, then by sampling in the subsequent dialysis process. The final formulation was investigated with small angle x-ray (SAXS) and neutron (SANS) scattering, dynamic light scattering (DLS) and cryo-TEM. The effect on structure was investigated for LNPs with a benchmark lipid composition and containing different cargos: calf thymus DNA (DNA) and two model mRNAs, polyadenylic acid (polyA) and polyuridylic acid (polyU). The LNP structure evolved during mixing in the microfluidic channel, however was only fully developed during the dialysis. The colloidal stability of the final formulation was affected by the type of incorporated nucleic acids (NAs) and decreased with the degree of base-pairing, as polyU induced extensive particle aggregation. The main NA LNP peak in the SAXS data for the final formulation were similar, with the repeat distance increasing from polyU<polyA<DNA, following the expected extent of base-pairing.

* Corresponding author.
E-mail address: tommy.nylander@fkem1.lu.se (T. Nylander).
https://doi.org/10.1016/j.jcis.2023.12.165
Received 23 October 2023; Received in revised form 22 December 2023; Accepted 28 December 2023
Available online 5 January 2024

1. Introduction

The development of lipid nanoparticle (LNP) based therapeutics for delivery of RNA has become increasingly widespread in recent years, beginning with the approval of Onpattro for siRNA delivery and more recently, with the approval of two mRNA LNP vaccines during the SARS-CoV-2 pandemic. [1–4] The development of new strategies and materials, such as high throughput microfluidics based formulation and cationic ionisable lipids, have begun to address challenges associated with LNP development, such as scalability, efficacy, encapsulation efficiency and toxicity of LNP components. [5,6] As a result, this has become a rapidly expanding field, with a large push for the optimisation of lipid formulation composition and development of new lipids and lipidoids to optimise function *in vitro* ([7–10], [1] and ref.s within, [5] and ref.s within). Despite this, there remains a lack of understanding of the mechanism of action of these LNPs and their structure-function-efficacy relationship. Typically LNPs have been described as a 'delivery platform', implying that they are insensitive to the encapsulated cargo. It is, however, becoming increasingly clear from work over the last few years, that LNPs containing short chain nucleic acids (NAs), such as siRNA and antisense oligonucleotides, form very different structures to those containing longer chain mRNA. [11–17] Within that margin, the question then arises of the sensitivity of the system to other factors, such as sequence of the encapsulated NA and/or structure, as changes in internal structure have been discussed with respect to these factors. [18,19] Structural characterisation has also typically been in terms of the internal LNP structure and limited to size and morphology characterisation with dynamic light scattering (DLS) and cryo-transmission electron microscopy (cryoTEM), respectively. [20] In this study, we have followed and characterised the structure of LNPs throughout the formulation process, which is composed of three main steps:

1. Mixing of the lipid solution in ethanol and low pH aqueous solution containing the NA cargo in a microfluidic chip or T junction mixer.
2. Dialysis of this mixture to remove the ethanol and change the buffer to phosphate buffered saline (PBS), thereby increasing the pH and the salt concentration.
3. Concentration of the dialysed formulation via centrifugation to produce the final formulation.

Extensive changes in structure and sample composition (i.e. separate solutions to NA-lipid complexes to final LNPs) occur during these stages. It is key to understand and rationalise these changes, in order to optimise the formulation process and understand the effects of different conditions on the final formulation, such as type and concentration of cargo. As it has been extensively shown in the literature that the structure of these LNPs is strongly dependent on the lipid formulation, [11–15,21,22] in this work we have chosen to use a benchmark lipid composition containing DLin-MC3-DMA (MC3):cholesterol:DSPC:DMPE-PEG2000 in the ratio 50:38.5:10:1.5. With this lipid composition, we have investigated the structure of a series of LNP formulations containing different cargos: calf thymus DNA (DNA) and two model mRNAs, polyadenylic acid (polyA) and polyuridylic acid (polyU). For the mRNA cargos polyA and polyU, two different cargo concentrations N:P 3 and 6 were characterised, where N:P is the MC3 nitrogen (N) to nucleotide phosphate (P) ratio and N:P 3 is a higher NA loading than N:P 6. The structure of these LNPs was elucidated using a combination of orthogonal techniques including small angle neutron and x-ray scattering (SAN/XS) and cryoTEM, which have previously been shown to provide detailed structural information for mRNA LNPs.

2. Results and discussion

2.1. The structure evolves during mixing in the microfluidic channel

During the first step of formulation, microfluidic mixing, for two formulations, DNA N:P 3 and polyA N:P 3, SAXS data were collected at four different positions in the microfluidic channel at three points along the staggered herringbone geometry and one at the outlet (the channel is highlighted in Fig. 1A, with the full chip shown in Fig. 1B), in order to follow the structural changes occurring through the initial mixing stage. The use of *in situ* SAXS measurements and a microfluidic device allowed us to follow the LNP structural evolution with time. The junction of the 2 inlets here represents time zero and as the solutions enter the channel, mixing of the 2 solutions occurs. This is associated with dilution of ethanol in the aqueous solution and consequently a decrease in lipid solubility that provides the driving force for the lipids to self-assemble. At the same time the protonation of MC3 promotes its association with the negatively charged nucleic acid.

During this time, for both the DNA N:P 3 and polyA N:P 3 samples, a growth of a shoulder at $q \approx 0.01 - 0.03$ Å^{-1} was observed, which grows moving further along the microfluidic channel (Figs. 1C,D). Previous work with this lipid composition by Li et al. [22] indicated the formation of 'protoLNPs' containing the helper lipids DSPC, DMPE-PEG2000 and cholesterol (with or without NA) and NA-MC3 complexes without any helper lipid after mixing in a T junction mixer. Similarly, Yanez-Arteta et al. [15] observed 'vesicle like' structures with more electron dense parts after initial formulation with a staggered herringbone mixer. It is likely that this growing shoulder is a result of strong aggregation between the lipid and NA components, with higher intensity as more of these 'protoLNPs' and lipid-NA complexes form.

Kulkarni et al. [12] also saw these small vesicle-like structures and some electron dense structures in a comparable LNP formulation with DLin-KC2-DMA (KC2) as the ionisable lipid and siRNA. These initial structures appear to be similar, although there are clear differences in LNP self-assembly with KC2 in comparison to MC3, i.e. no internal structure is observed without RNA for LNPs with KC2. Similar structures were also observed in later work with LNPs formulated with KC2 and containing pDNA and mRNA. [13]

Notably, for DNA N:P 3, a broad peak around $q \approx 0.12$Å^{-1} was visible at the outlet, indicating that a relatively ordered structure with a repeat distance of 58 Å had already formed before dialysis for this sample. Although it is not possible to assign the structure from a single peak, this repeat distance is comparable to the one observed for the final LNP formulation, indicating that this is likely related to the final core structure. For the polyA sample, however, a peak was not observed at the outlet, which could be a result of low signal (due to the depth of the microfluidic channel) and/or that the formation of the ordered structure for polyA is slower. Here we note that about 30 ms is required for the dispersion to pass the channel. A slower formation of the internal structure peak was also observed by Yu et al. [18] for polyA than pDNA, when mixing with monoolein/SM-102, with a more intense peak observed for pDNA, although we cannot exclude the possible influence of the lower ionic strength of the buffer used for the polyA sample.

2.2. The LNP structure is only fully developed during the dialysis

In the second formulation step, the samples produced by microfluidic mixing were dialysed against phosphate buffered saline (PBS), in order to reduce the amount of ethanol present and have physiologically acceptable solution conditions for intravenous administration. Further SAXS data (shown in Figs. 1E-H) were collected throughout the dialysis step of the formulations containing DNA N:P 3 and polyA N:P 3, with an additional sample of polyU N:P 3, in order to understand the changes occurring in the internal structure.

A peak at approximately 0.12 Å^{-1} was observed for all three samples when the first SAXS measurement was performed after 7 h (Fig. 1F-H). The q positions were similar to those for the final formulations, indicating that the internal structure corresponding to this peak had already formed.

A change in peak position was observed throughout dialysis, in which the repeat distance decreases to a minimum after 12 hrs of dialysis, before increasing again to a maximum after the full dialysis time

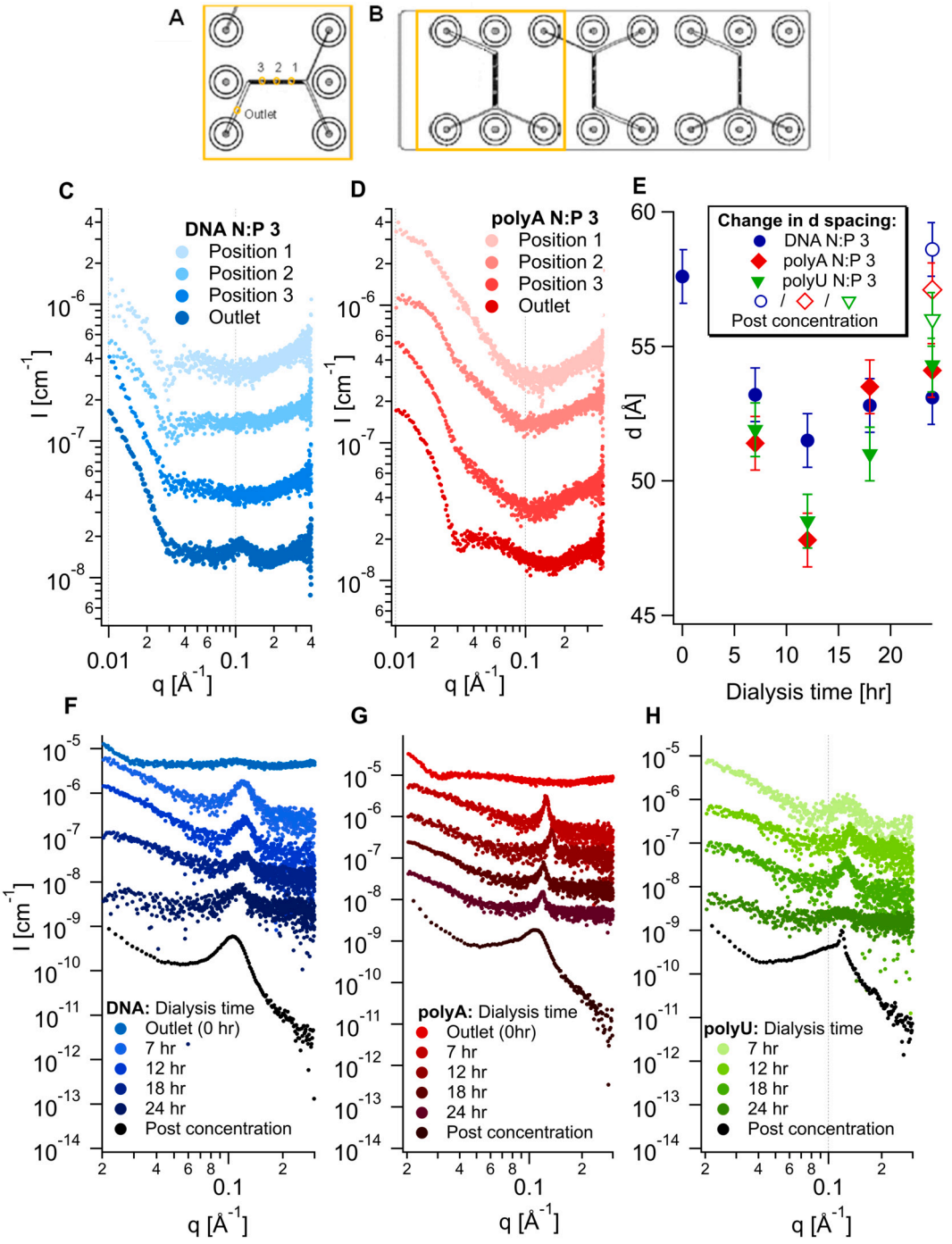

Fig. 1. SAXS measurements during the LNP formulation process demonstrated the evolution of the structure. SAXS data were measured during microfluidic mixing at 4 points along the microfluidic channel (A) in a staggered herringbone mixer (B). Data is shown for LNPs containing (C) DNA N:P 3 and (D) polyA N:P 3. (E) The evolution of the repeat distance during dialysis was calculated from the peak positions in SAXS data for LNP formulations containing (F) DNA, (G) polyA and (H) polyU N:P 3. The SAXS curves presented in C,D and F – H are offset for clarity.

(Fig. 1E, S1, Tables S1-3). This trend appears to be the same regardless of the cargo, indicating that it is most likely happening due to general changes in the LNP structure.

During the dialysis, there are multiple processes occurring simultaneously, which could all contribute to the change in peak position. These include (i) removal of ethanol from the system, (ii) particle fusion, and (iii) exchange of buffer ions as well as an increase of the bulk pH and salt concentration as the formulations were dialysed against PBS.

(i) Removal of ethanol will result in a further reduction in solubility of the lipids in the solvent, thereby driving their self-assembly further. This process occurs very fast and would likely only affect the earliest stages of dialysis.

(ii) Previous work [11,14,22] has shown that, during the dialysis, fusion of the protoLNPs with each other and with NA-MC3 complexes to obtain the final LNP formulation occurs. This would result in changes in lipid composition and distribution throughout the LNP structure, such as changes in curvature due to change in partitioning of cholesterol between the LNP core and shell.

(iii) Exchange of buffer ions will increase the pH in the dispersion, thereby reducing the proportion of protonated MC3, which in turn could affect ion mediated NA-lipid interactions. Deprotonation

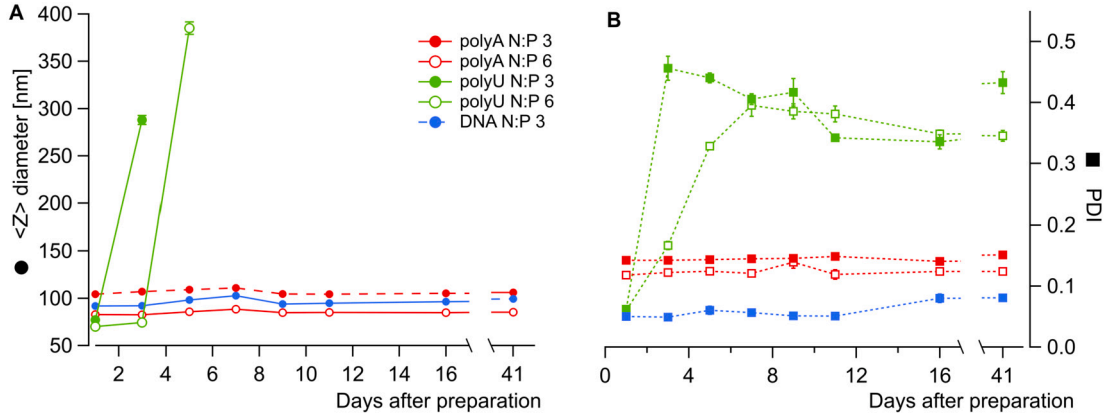

Fig. 2. DLS data for stability measurements of DNA N:P 3, polyA N:P 3 and polyU N:P 3 showing the mean diameter (A) and PDI (B) over 41 days, during which the samples were stored at 4°C.

of the MC3 head group with increasing pH would result in reduced electrostatic repulsion between the MC3 head groups and increased curvature towards the water phase. This deprotonation and increase in salt concentration to 150 mM NaCl would also affect the NA-MC3 interaction [23]. The reduced charge on the MC3 head group and increase in screening of electrostatic interactions, provided by the higher ionic strength, could result in a weaker interaction between the MC3 headgroup and NA backbone. In previous work with a model system composed of MC3/DOPC, however, adsorption of NAs was observed even above the apparent pKa of MC3, showing that there is still a non-negligible interaction between the NA and MC3 head group, even when the majority of MC3 is assumed to be deprotonated. [24]

It should be noted, however, that dialysis is not a scalable process, therefore for large scale manufacturing, alternative less time consuming methods, such as tangential flow filtration (TFF), are used instead. [25, 26] As these methods can change the solution conditions much more quickly than dialysis, the kinetically controlled rearrangement of the sample is most likely affected.

2.3. Small effects of the type of incorporated nucleic acid on the complex formation with MC3 and LNP structure

The differences in the shapes of the peaks at q ≈ 0.12 $Å^{-1}$ observed during dialysis for DNA, polyA and polyU N:P 3 (Fig. 1F-H) could also potentially be linked to the differences in nucleic acid structure, as well as difference in sequence. For DNA (Fig. 1 F), the peak is broader than the sharp peak observed for polyA (Fig. 1 G) but for both DNA and polyA, it remains well-defined for the full dialysis. Although small changes in peak position occur for the polyA and DNA samples, no major changes to the peak width or shape were observed. Both DNA and polyA would be expected to be dominated by double helical structures upon initial mixing, where the sharpness of the polyA peak is potentially related to the rigidity and lack of sequence variation of the polyA, compared to the more varied sequence of DNA as discussed previously. [18,27] The initial complexation between MC3 and polyA is expected to occur when a significant proportion of the polyA is in its double helical form. This complexation in combination with the confinement in the LNP could prevent or at least hamper a structural change to a single stranded helix polyA at the higher pH after dialysis.

The peak shape for polyU (Fig. 1 H), on the other hand, undergoes a series of changes during dialysis. Initially the peak is relatively sharp, similar to that of polyA, but becomes very broad by the end of the dialysis time. The initial phase of complexation of polyU is expected to be driven by electrostatic association with the oppositely charged MC3, where the structural order is provided by the MC3 self-assembly and charge neutralisation. However, as the pH increases during the dialysis and the proportion of charged MC3 decreases, the electrostatic interaction is weakened and the hydrophobic interactions becomes more important. The entropic cost of limiting the polyU random coil motion becomes more important, which altogether results in a less ordered system.

For all the samples after they are formed, the position of the main NA LNP peak in the SAXS data for the final formulation were similar, with the repeat distance increasing from polyU<polyA<DNA, although with a notably broader peak in the case of polyU. It could be argued that this trend follows the expected extent of base pairing/double vs single stranded forms, with the larger repeat distance observed for DNA, mostly base paired, and the smallest for polyU, single stranded. The effect of the increased linear charge density for a double stranded structure on the polarity of the MC3 head groups could also result in a similar increase.

2.4. Structure and composition of the final LNP formulation with different nucleic acid cargos

The structure of the final LNP formulation after concentration was elucidated by combining the information from SANS, revealing LNP shape, size and composition; cryoTEM, which provides insight on particle morphology; and SAXS, which provided high resolution information on the internal structure.

2.4.1. Colloidal stability of the final formulation was affected by the type of incorporated nucleic acids

Initial characterisation of the particle size by DLS measurements (Fig. 2) showed that for both polyA and polyU, the LNP size upon formulation was smaller for the higher N:P ratio (i.e. for the lower NA concentration), which has previously been reported in literature. [15,22]. The DNA N:P 3 and polyA samples with both N:P ratios were colloidally stable over the measured period of 41 days when stored at 4°C. For polyU, both N:P ratio samples aggregated very soon after formulation (Fig. 2), shown here by an increase in both the intensity weighted mean size (<Z> diameter) and polydispersity index (PDI, indicating the width of the size distribution). It should be noted that, for a high PDI and multimodal size distribution as in the case of polyU samples with N:P 3 and N:P 6 after 1 and 3 days, respectively, the value of the diameter would not be representative of the sample and were therefore not plotted.

In the SANS data for the DNA N:P 3 and the polyA N:P 6 samples, there was no significant upturn in the low-q region (although this is somewhat limited by the available q range, as shown in Fig. 3B,E), which is consistent with the lack of change in size observed in DLS (Fig. 2A). In the SANS data for poly A N:P 3, a minor upturn was noted (Fig. 3A), although no change in size was observed with DLS. It should be noted, that there is a small upturn for the polyU N:P 3 and 6 samples at the lowest q values (Fig. 3C,D), which can be seen more clearly

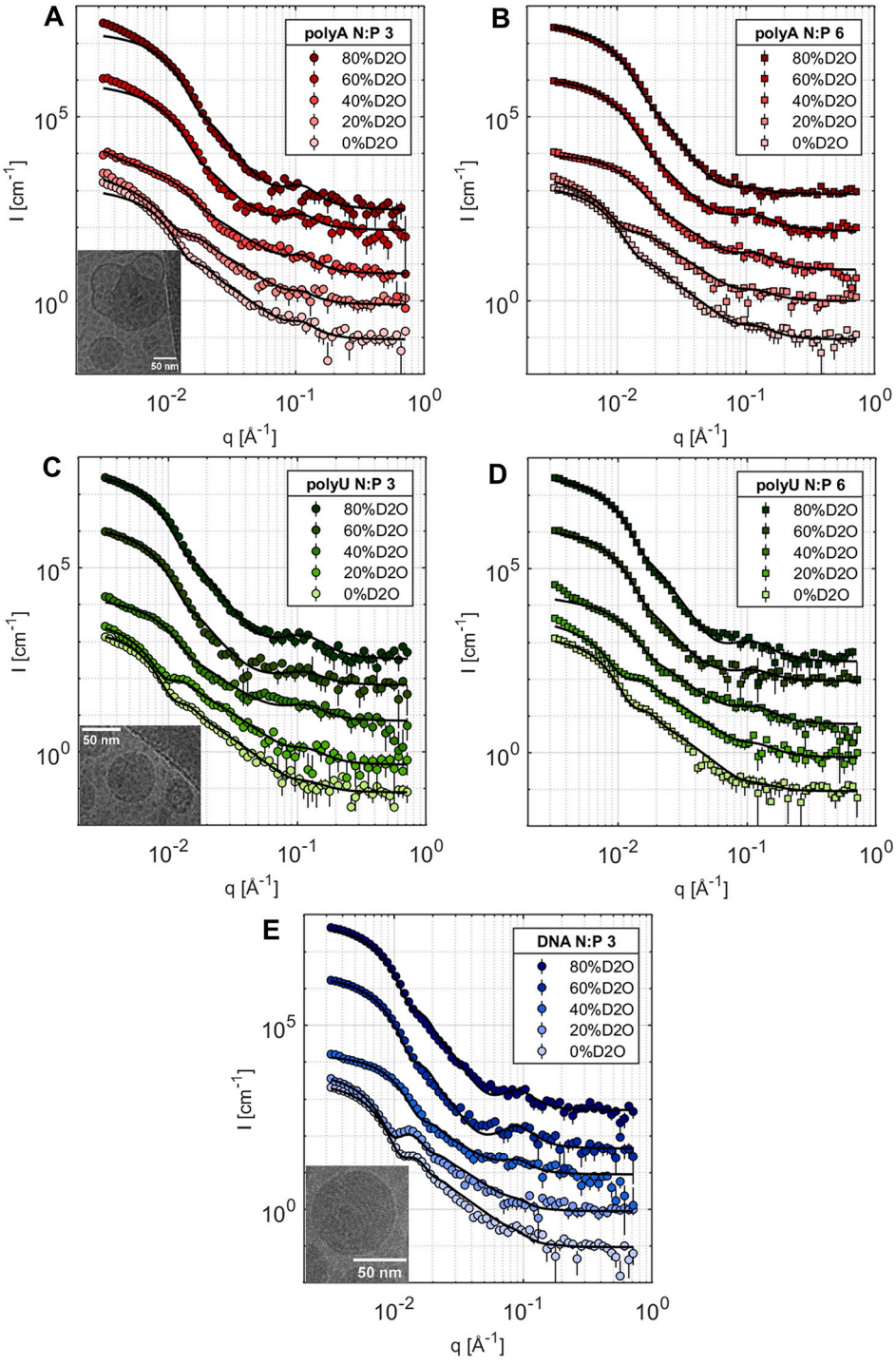

Fig. 3. SANS data collected for LNPs containing polyA N:P 3 (A) and 6 (B), polyU N:P 3 (C) and 6 (D) and DNA N:P 3 (E). All samples were measured in five different solvent contrasts: 0, 20, 40, 60, 80% D_2O (plotted with light to dark colours for increasing D_2O amount). All samples were fitted with a combined core shell sphere and broad peak model (black lines) and the data is offset for clarity. In the insets of A, C and E, cryoTEM images for these samples are included, highlighting LNP populations of interest.

in the corresponding Guinier plots (Figure S5C,D), due to the extensive aggregation observed in the DLS data (Fig. 2). It is possible that the larger aggregates observed with DLS sedimented during the measurement time and the remaining particles had a smaller and more uniform size.

The change of the colloidal stability of the formulation was the most striking difference observed by encapsulating different types of nucleic acid cargos. For the DNA and polyA samples, both DLS data and SANS indicated that the formulation was stable over the time measured. For the polyU samples, however, massive aggregation occurred almost immediately after dialysis, with a slightly slower onset for N:P 6 than N:P 3. This difference in stability could be related to the structure of these NAs. PolyU is expected to be present as a random coil over the solution conditions used here, [28,29] whereas polyA undergoes a series of structural changes over the pH range used in formulation. At physiological pH and temperature, polyA exists as a single stranded helix with random coil domains, but as the pH decreases these assemble into double helices (at ≈pH 6.5), which become more rigid, ordered and tightly

Table 1
Structural information on NA LNPs as determined by SANS, where vf_{shell} and vf_{core} are the volume fractions of solvent in the shell and the core, respectively.

Sample	vf_{shell}	vf_{core}	Core radius/Å	Shell thickness/Å	PDI (Schulz)
polyA N:P 3	0.37±0.09	0.33±0.05	215±1	45±1	0.23
polyA N:P 6	0.39±0.09	0.17±0.03	210±1	50±1	0.28
polyU N:P 3	0.32±0.09	0.43±0.05	295±1	49±1	0.22
polyU N:P 6	0.4±0.1	0.29±0.09	242±1	49±1	0.22
DNA N:P 3	0.1±0.2	0.29±0.05	288±1	48±1	0.17

packed (below pH 5-5.5) and result in a slow gel formation over time. [29–32] Although the base pairing for the DNA sample could be affected by the low pH of the formulation buffer, it is likely to still have extensive base pairing. The LNPs containing DNA and polyA, which are expected to have the higher proportion of double stranded structures, were the most colloidally stable, whereas the samples containing polyU, which exists as purely single stranded polymers, aggregated quickly. High colloidal stability, however, for mRNA LNPs with this lipid composition has been established and mRNA is most commonly present as a single stranded molecule. Due to its high flexibility, dynamic base pairing between sections of the mRNA strand occurs and can result in incredibly complex secondary and tertiary structures. Here polyU represents an extreme case, whereas it is more probable that an mRNA strand would be base paired to some extent. [33,34]

2.4.2. LNP size and shape – determining the form factor

Previous structural characterisation of this lipid composition with mRNA by SANS in studies by Yanez Arteta et al. [15] and Sebastiani et al. [16] has shown that these LNPs have a core-shell structure, with a distinctly different lipid composition in the core and shell, and a peak at ≈ 0.1 Å^{-1} corresponding to the internal structure. The structured core is composed of MC3, cholesterol, aqueous solvent and, assuming the LNP is not empty, the RNA cargo, whereas the outer shell contains DSPC, the DMPE region of the PEG lipid, cholesterol and MC3. [15,16] As this internal structure peak was also visible here, the SANS data was fit using a core-shell sphere model plus a broad peak model (CSS+BP), as previously described. [16] For each sample, the radius and shell thickness were constrained to be the same for the five different solvent contrasts (0, 20, 40, 60, 80% D_2O) and fit simultaneously, whereas the SLDs of the core (SLD_{core}) and shell (SLD_{shell}) were allowed to vary individually for each contrast. The use of cholesterol with a high degree of deuteration increased the contrast between the shell and core and by comparing the fitted values for the same sample measured in different solvent contrasts, it was possible to calculate the volume fractions of solvent in the core (vf_{core}) and shell (vf_{shell}) and the dry SLDs of the core ($SLD_{dry-core}$) and shell ($SLD_{dry-shell}$) using the following relationship:

$$SLD_{wet} = (vf_{solvent} SLD_{solvent}) + ((1 - vf_{solvent}) SLD_{dry}) \quad (1)$$

The results are summarised in Table 1 and further details on the fitting procedure and compositional analysis can be found in the SI (Tables S4-7). The data for all 5 samples were well described by this model, demonstrating that the core-shell sphere structure previously observed for mRNA LNPs is also relevant for these cargos. [15,16] This is also supported by the changing peak position in the distance distribution functions P(r) (Figure S6, S7, Table S5) with solvent contrast, as the shell is matched out at higher D_2O. In general, the fitted values for the radius and shell thickness (Tables 1, S6) agreed well with those observed in cryoTEM (inset of Figs. 3A,C,E and Figures S2-4) and DLS measurements (Fig. 2). It is important to bear in mind that DLS measures the hydrodynamic diameter and therefore the particle size from DLS also includes the solvation shell. These values should, therefore, be larger than those obtained from SANS measurements, corresponding to the radius of gyration R_g, which are compared in Table S5. We also note that the size from DLS is quoted as the mean of the intensity weighted distribution, therefore it is biased to larger sizes for the particles when the polydispersity of the sample is >0.1. Additional SANS data at 37°C were collected for the samples discussed here (Figure S8) and at higher temperature for the stock LNP solutions (Figure S9), but no significant changes were observed with temperature.

2.4.3. LNP lipid composition

From the SANS fitting, the lipid molar fractions for the core and shell were estimated (Table 2) and were remarkably consistent across the different cargos with the same N:P, implying that, despite the larger solvent volume fraction in the shell for polyA and polyU, the lipid composition of the shell and core was very similar for these systems. The main difference observed between the compositions of the samples was that the solvent volume fraction decreased and the mol% MC3 increased in the core with increasing N:P, effectively maintaining the input N:P ratio in the core. This increased %mol MC3, while mol% cholesterol remained almost unchanged, would result in an overall lower curvature of the core lipids towards the water phase. This trend is consistent with the larger repeat distance observed for empty LNPs in SAXS.

2.4.4. LNPs with incorporated nucleic acids coexist with empty LNPs

As it was only possible to describe the internal structure peak in the SANS data with a generic broad peak model, due to lower resolution and larger errors, SAXS measurements of the LNP stock solutions (LNP concentration ≈ 20 mg/mL) were performed, in order to interrogate the peak, and therefore LNP internal structure, in more detail.

Typically, when discussing the internal structure of LNPs, it has been assumed that the LNP population is homogeneous, however previous work by Li et al. [22] and Sych et al. [35] has shown that the number of RNA molecules encapsulated per LNP is in fact a distribution, which becomes broader with decreasing N:P. Both studies also found that there is a large proportion of empty LNPs without any RNA molecules inside, with either no change [22] or an increase [35] in proportion of empty LNPs with N:P.

In previous work by Yanez-Arteta et al. [15], it was shown that the internal structure peak for empty LNPs was much less well-defined and shifted to a lower q than the equivalent peak in a formulation containing EPO RNA (N:P 3). It is therefore likely that there is a significant contribution to the SAXS pattern from the empty LNP internal structure.

Here (Fig. 4), the peaks in the SAXS data for the N:P 6 samples (Fig. 4B,D) are broader and the peak is less prominent than the corresponding N:P 3 peak for the same cargo (Fig. 4A,C), potentially due to a larger contribution from scattering from the empty LNP internal structure.

The data from the NA LNPs was fitted with a linear combination of a broad peak model describing the empty LNP internal structure and either 1 or 2 Gaussian peaks, describing the NA LNP internal structure. SAXS data for the empty LNP was first fitted using a generic broad peak model (Figure S10, Table S8). The NA LNP SAXS data was then fitted using a linear combination of this broad peak model, with all except the scaling parameters fixed from the empty LNP fit result, and the Gaussian peak(s), for which all parameters were allowed to vary (Fig. 4, Tables S9, S10).

Both the polyA samples (Fig. 4A,B) and polyU N:P 6 (Fig. 4D) were well-described by the single Gaussian peak model, however for polyU

Table 2
Lipid composition of the shell and core of NA LNPs as determined by SANS. *The position of these components was fixed so that the DSPC and DMPE portion of the PEG lipid were present in the shell and the NA cargo (nt = nucleotides) was present in the core.

Model: CSS+BP	%mol in shell				%mol in core		
Sample	**MC3**	**Chol**	**DSPC***	**DMPE***	**MC3**	**Chol**	**NA (nt)***
polyA N:P 3	18±2	60±5	19.7	3.0	65±2	13±4	22.3
polyA N:P 6	10±4	67±7	19.9	3.0	78±4	8±6	13.9
polyU N:P 3	15±3	63±5	19.9	3.0	68±2	11±4	21.1
polyU N:P 6	13±5	64±9	20.4	3.1	76±4	13±7	11.3
DNA N:P 3	19±3	59±7	19.1	2.9	64±3	12±6	23.7

N:P 3 (Fig. 4C) an additional Gaussian peak was included to describe the Bragg peak at approximately 0.12$Å^{-1}$.

For the polyA samples (Fig. 4A,B), the position and width of the peak for both N:P was the same within the fitting error (Fig. 4F). Here only the scale of the single peak relative to the empty LNP contribution decreased with increasing N:P (Table S9, Fig. 4G). In the case of polyU N:P 3 (Fig. 4C), two Gaussian peaks were required; one broader peak at 0.112$Å^{-1}$ and a second very narrow one describing the Bragg peak at 0.119$Å^{-1}$ (Table S10, Fig. 4F). PolyU N:P 6 (Fig. 4D) on the other hand could be fitted with a single peak, matching the position and width of the broader peak seen for polyU N:P 3 (Table S9, Fig. 4F).

An additional Gaussian peak for the DNA sample (Fig. 4E) was introduced in order to better describe the shoulder on the high q side of the peak. The sample was well described by this combination of two Gaussian peaks, one with the peak position at the q with maximum intensity value and a second, broader peak at higher q (Table S10, Fig. 4F). This indicates the coexistence of multiple populations of LNPs with different internal structures, which could correspond to a combination of empty LNPs and NA LNPs with a different number of DNA molecules inside.

For the polyA and polyU samples, however, (excluding the contribution from the Bragg peak for polyU N:P 3) the same peak could describe both the N:P 3 and 6, but with a lower scale factor for the NA LNP contribution for N:P 6 compared to the contribution from empty LNPs (Fig. 4G). This implies that the NA LNP population for polyA and polyU is more homogeneous. In previous work with this lipid composition, Li et al. [22] showed that the number of mRNA molecules per LNP doubled when the length of the mRNA used was halved, indicating that LNPs have a maximum mass limit, i.e. number of bases, rather than a maximum molecule number limit. This would result in well-defined populations of LNPs based on number of NA molecules per LNP for an NA of well-defined length, which is more relevant to the DNA samples here with a length of 587 - 831bp. The polyA and polyU used here, however, were very polydisperse with reported lengths of 2200 – 11,000 nt (700 - 3500 kDa) and 350 - 3500 nt (100 - 1000 kDa), respectively, resulting in a wider range of possible number and mass of NA molecule per LNP.

2.4.5. LNP shape and morphology

For all samples in the cryoTEM images, the majority of the sample populations appear as relatively uniform spheres with an electron dense core, as observed in previous work. [15] For both the polyA N:P 3 and polyU N:P 3 samples, however, additional populations can be observed.

In cryoTEM images for LNPs with polyA N:P 3 (Figure S3), a small number of the LNPs appear to have blebs at the surface, which could account for both the relatively large polydispersity required to describe the SANS data for this sample and the larger solvent fraction in the shell compared to the DNA N:P 3 sample. These have been seen in similar mRNA-LNP systems, usually as a result of high buffer concentrations in the early stages of formulation and were theorised to contain the mRNA strand after dialysis. [14]

In the polyU N:P 3 sample (Figure S4), both the fitting of the SAXS data with two very different Gaussian peaks and the cryoTEM images, in which a small number of hollow ellipsoids with an electron dense shell can be observed alongside the expected LNPs, indicate the presence of at least two populations. As both polyU samples had already aggregated at the time of the SANS measurement, it was surprising that the fit values and subsequent calculated lipid compositions, were as similar as the other samples and could be described with such a low polydispersity. This could be a result of LNPs with a different lipid composition being unstable, resulting in their aggregation and sedimentation, leaving LNPs with the expected lipid composition to be measured. This is further supported by the cryoTEM images, in which the larger population of LNPs appears very similar to the DNA samples and most likely corresponds to the broad peak observed in the SAXS fit. It cannot be ruled out, however, that these structures are also an effect of the blotting procedure.

3. Conclusion

In this work, we have shown that the LNP structure evolves during the mixing in the microfluidic channel, but is only fully developed during the dialysis step, which to our knowledge is the first time this has been shown with SAXS. The main effect of the type of nucleic acid cargo was on the colloidal stability of the LNPs, with a lower stability observed for NAs with a larger proportion of single stranded structures, although no effect was observed on the lipid composition. A change in lipid composition was instead observed with N:P, where the molar ratio of MC3 in the core increased with the higher N:P. The SAXS data for the final formulations showed that the NA LNP samples contained at least two populations of particles, one with and another without nucleic acids. For all the samples, a small decrease in contribution from the NA internal structure and increase in contribution from the empty LNP peak was observed for each cargo with increasing N:P. This agrees well with data from previous work, [22,35] although more detailed characterisation would be required to interpret this in terms of distribution of LNPs with different nucleic acid loads. Understanding the full complexity and heterogeneity of LNP formulations is vital to be able to optimise formulation components and conditions and drive the rational design of these systems.

4. Materials and methods

4.1. Materials

1,2-distearoyl-sn-glycero-3-phosphocholine (DSPC, powder) and cholesterol (powder) were purchased from Avanti Polar Lipids, 1,2-dimyristoyl-snglycero-3-phosphoethanolamine-N-[methoxy(polyethylene glycol)-2000] (DMPE-PEG2000) was purchased from NOF Corporation and (6Z,9Z,28Z,31Z)-heptatriacont-6,9,28,31-tetraene-19-yl 4-(dimethylamino)butanoate (DLin-MC3-DMA or MC3, oil) was purchased from Biorbyt. DNA solution from calf thymus (10 mg/mL in 100 mM phosphate buffer pH 7), polyadenylic acid (powder), polyuridylic acid (powder) and all buffer salts were purchased from Sigma Aldrich. Deuterated cholesterol d-45 (85% D) was produced by the National

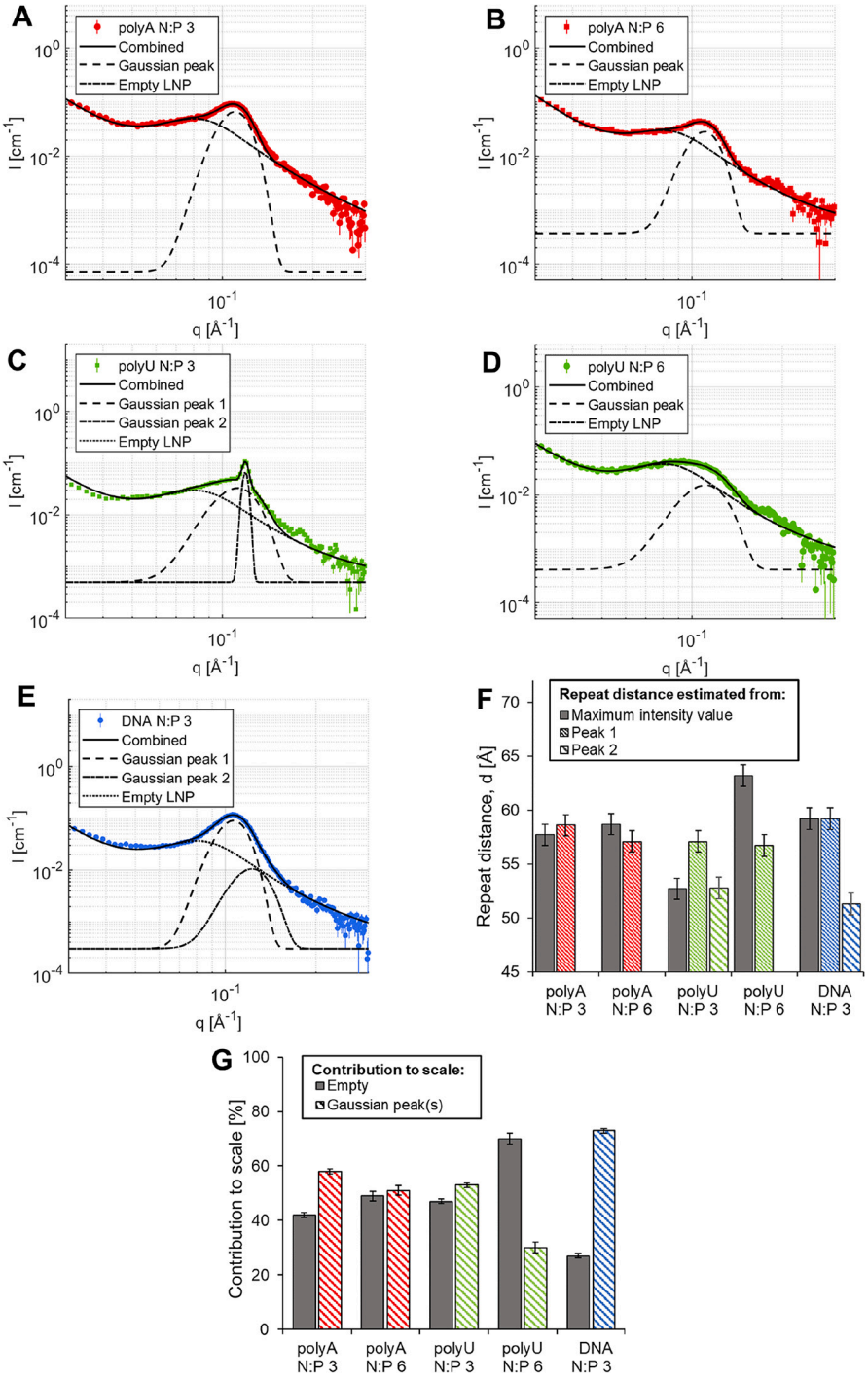

Fig. 4. Static SAXS data was fitted using a broad peak model with either a single Gaussian peak for LNPs containing polyA N:P 3 (A) and 6 (B) and polyU N:P 3 (C) and 6 (D) or two Gaussian peaks for LNPs containing dsDNA N:P 3 (E). A comparison between the repeat distance as estimated from the maximum value of the peak in the SAXS data and estimated from the position of the fitted peaks is presented in (F). The relative contributions of the scale factor for the peaks corresponding to empty LNPs and NA LNPs are presented in (G).

Deuteration Facility (ANSTO) as previously reported. [16] Phosphate buffered saline (1x PBS, 155 mM NaCl, 1.06 mM KH_2PO_4, 2.97 mM Na_2HPO_4, pH7.3) was prepared using Milli-Q purified water (18 MΩ cm) or D_2O from Sigma Aldrich.

4.2. Preparation of sample solutions

Stock solutions of 20 mg/mL of each lipid were prepared in 99.5% ethanol, mixed to the molar ratio 50/38.5/10/1.5 MC3/cholesterol/DSPC/DMPE-PEG2000 and diluted with 99.5% ethanol to 12.5 mM lipid (≈ 7.5 mg/mL). For SANS, DLS and in house SAXS measurements, the samples were prepared with d-45 (85% D) cholesterol, whereas for *in situ* SAXS and dialysis measurements, hydrogenous cholesterol was used. DNA was diluted in 50 mM citrate buffer pH 3.0 and polyA and polyU were dissolved in 2.5 mM HCl. In this work, two MC3 to nucleotide ratios (N:P) were investigated; for N:P 3, [NA] was 0.21 mg/mL and for N:P 6, [NA] was 0.11 mg/mL.

4.3. Preparation of LNPs

The lipids in ethanol and aqueous NA solutions were mixed in a Fluidic 187 Herringbone Mixer (COP) from Microfluidic ChipShop at a flow ratio of aqueous:lipid of 3:1 using a Harvard Apparatus Model 33 twin syringe pump and a total flow rate of 12 mL/min. The first and last 0.5 mL of the formulation were discarded. The formulations were transferred to MWCO 6-8 kDa Spectra/PorTM 1 dialysis membrane and dialysed overnight against 2 L 1x PBS at 4 °C with light stirring. The dialysed formulations were transferred to 50 mL Falcon tubes with an Amicon Ultra-15 10 kDa NMWL filter unit and centrifuged at 4000 g until [LNP] ≈ 20 mg/mL lipid. Encapsulation efficiency of all samples was measured using the RibogreenTM assay (Invitrogen) [36] and is reported in Table S11.

4.4. In house small angle X-ray scattering (SAXS) experiments

SAXS measurements of the final formulation ([LNP] ≈ 20 mg/mL lipid) were performed on a SAXSLab Ganesha 300XL (SAXSLAB ApS, Skovlunde, Denmark) with a 2D 300K Pilatus detector (Dectris) and Genix 3D x-ray source (λ_{x-ray} = 1.54 Å). Samples were sealed in reusable capillaries (diameter = 1.5 mm), which were mounted in a sample block which was kept at constant temperature with an external water bath. Data was collected over a q range of 0.001 – 0.75 $Å^{-1}$ for 2 hrs at 25 °C. The 2D scattering pattern was radially averaged using SAXSGui software to obtain I(q) and the solvent background was subtracted in Matlab.

4.5. Synchrotron SAXS: in situ mixing and dialysis

The *in situ* SAXS characterisation of the LNP formulation and dialysis was performed on CoSAXS at MAX IV using a wavelength of 1 Å, a beam size of 50 x 60 μm^2 (width x height) focussed at the sample position and an Eiger2 4M SAXS detector at a sample-to-detector distance of 3.044 m. For the *in situ* mixing, the microfluidic chip was mounted on a custom sample holder and the temperature monitored using a thermocouple throughout the experiment (T = 24.5 ±0.2 °C). SAXS measurements during mixing were performed at 4 different positions along the microfluidic channel, where three were along the herringbone geometry and one was at the outlet (Figure 1A). For each point along the channel, 500 frames with an exposure time of 20 ms were collected to follow the structural changes during mixing. As in the usual formulation procedure, lipids in ethanol and aqueous NA solutions were mixed in a Fluidic 187 Herringbone Mixer (COP) from Microfluidic ChipShop at a flow ratio of aqueous:lipid of 3:1 using a NEMESYS low pressure syringe pump (Cetoni GmbH) and a total flow rate of 12 mL/min. The channel depth was 0.2 mm, the channel width at the inlet was 0.3 mm and the channel width in the mixing section and outlet was 0.6 mm. The sample was collected and transferred to a dialysis chamber with 3.5 kDa cut off membrane in 2 L of 1x PBS. The samples were dialysed over 24 hrs with aliquots of 100 µL were extracted from the dialysis chamber for static SAXS measurements after 7, 12, 18 and 24 hrs. For static SAXS measurements of the samples over the dialysis period, the samples were loaded into reusable capillaries (diameter = 1.5 mm), which were mounted in a sample block with the temperature maintained at 25 °C by an external water bath. 63 frames with an exposure time of 20 ms were collected by scanning along the capillary in order to reduce the effect of radiation damage. The two-dimensional SAXS patterns were automatically reduced to 1D scattering patterns following calibration with silver behenate using Azint software provided by MAX IV [37] (https://github.com/maxiv-science/azint). The data was normalised using the incident and transmitted intensities with a custom python script in jupyter notebook. The frames were averaged together after exclusion of data sets with parasitic scattering (due to capillary flare). The solvent background was scaled such that the high q region (>0.25 $Å^{-1}$) matched the intensity of the sample and was subtracted in Matlab.

4.6. Dynamic light scattering (DLS)

DLS measurements were performed using a Zetasizer Nano ZS (Malvern Instruments Ltd.) with LNP stock solutions diluted to ≈0.04 mg/mL lipid. Samples were equilibrated at 25 °C for 120 s before measurement and the results of 6 measurements were averaged. The apparent hydrodynamic diameter was calculated using the Einstein-Stokes equation assuming a spherical particle and solvent viscosity of 0.8872 cP.

4.7. Small angle neutron scattering (SANS) experiments

All LNP samples were measured on the Sans2d diffractometer at the ISIS Neutron and Muon Source, using a wavelength range of 1.75 - 14.4 Å and two detectors at 4 and 8 m distance from the sample. The samples were measured over a q range of 0.0024 – 0.96 $Å^{-1}$ in 1 or 2 mm Hellma cuvettes mounted in a temperature controlled sample changer. Each LNP sample was measured at 25 °C and a concentration of 3.9 mg/mL in 5 different solvent contrasts: 1x PBS with 0, 20, 40, 60, 80% D2O, prepared by diluting the LNP stock samples in the appropriate ratio of 1x PBS prepared in 100% H2O and 1x PBS prepared in 100% D2O. An additional measurement was performed for each LNP sample ([LNP] = 3.9 mg/mL) in 0% D2O after equilibration to 37 °C. The LNP stock solutions ([LNP] ≈ 20 mg/mL, 0% D2O) were additionally measured after equilibration at 25, 37, 50 and 65 °C. Data for each solvent contrast at the corresponding temperatures were also measured.

All data was radially averaged, scaled to absolute intensity, merged and background subtracted (using the measured solvent background) using Mantid Workbench [38]. The data can be found at https://doi.org/10.5286/ISIS.E.RB1920532-1.

4.8. SAS data fitting

All the SAS data were analysed using SasView (version 5.05, https://www.sasview.org/) and further details for all SAS fitting are included in the SI.

4.8.1. In house SAXS

SAXS data for empty LNPs was kindly provided by Yanez Arteta et al. from reference [15] and was fitted using the broad_peak model in SasView with details on the fitting constraints given in the SI. The SAXS data for NA LNPs was fit using a combination of the broad peak model (describing the contribution from empty LNPs) and either one or two Gaussian peaks (describing the contribution from the internal structure of NA LNPs). The structural parameters from the broad peak model were fixed, with only the scaling parameters allowed to vary, and all of the Gaussian peak parameters were allowed to vary. For all samples, the data was fitted over the q range 0.028 – 0.75 A^{-1}.

4.8.2. In situ SAXS

Data measured during microfluidic mixing and dialysis were analysed using the broad peak model in SasView in a limited q range around the peak position. Parameters corresponding to peak scale, width and position were manually estimated, then fitted simultaneously. All other parameters were estimated and fixed.

4.8.3. SANS

Data for the same LNP samples but different solvent contrast (D_2O/H_2O) were fitted first to a core shell sphere (CSS) model over a limited q range. The core radius, shell thickness, SLD of the core and SLD of the shell were allowed to vary with all other parameters estimated and fixed. Radius and thickness were constrained to be the same for all solvent contrasts and fitted simultaneously, whereas the SLDs of the core and shell were fitted simultaneously for each contrast. Each sample was then fit with a combined model of the core shell sphere plus

a broad peak, to describe the contribution from the internal structure peak at ≈ 0.1 Å^{-1}.

For each sample, the combined model was fitted over the full q range. The CSS structural parameters were fixed to those determined from the initial CSS fit and the peak structural parameters were estimated from the sample SAXS data. The SLD of the core and shell and the broad peak scale parameters were then allowed to vary. From the fitted SLD values for the core and shell for each solvent contrast, the corresponding solvent volume fractions and dry SLDs of the shell and core were calculated. From these values, the lipid composition of the shell and core was estimated.

CRediT authorship contribution statement

Jennifer Gilbert: Conceptualization, Data curation, Formal analysis, Investigation, Methodology, Software, Supervision, Writing – original draft. **Federica Sebastiani:** Data curation, Validation, Writing – review & editing. **Marianna Yanez Arteta:** Methodology, Resources, Validation, Writing – review & editing. **Ann Terry:** Data curation, Formal analysis, Investigation, Supervision, Validation. **Anna Fornell:** Data curation, Resources, Visualization. **Robert Russell:** Resources. **Najet Mahmoudi:** Formal analysis, Investigation, Methodology, Writing – review & editing. **Tommy Nylander:** Conceptualization, Data curation, Funding acquisition, Project administration, Resources, Supervision, Validation, Writing – review & editing.

Declaration of competing interest

The authors declare that they have no known competing financial interests or personal relationships that could have appeared to influence the work reported in this paper.

Data availability

Data will be made available on request.

Acknowledgement

This work benefited from the use of the SasView application, originally developed under National Science Foundation, NSF, award DMR-0520547. SasView contains code developed with funding from the European Union's Horizon 2020 research and innovation programme under the SINE2020 project, grant agreement No 654000. The deuterated cholesterol used in this work was provided by the National Deuteration Facility, which is partly funded by the National Collaborative Research Infrastructure Strategy (NCRIS) – an Australian Government initiative. Research conducted at MAX IV, a Swedish national user facility, was supported by the Swedish Research Council under contract 2018-07152, the Swedish Governmental Agency for Innovation Systems under contract 2018-04969, and Formas under contract 2019-02496. We acknowledge the use of the "AdaptoCell for MAX IV Laboratory users" platform developed under the Swedish Foundation for Strategic Research, grant ITM-0375. The financial support from Swedish Research Council under contract 2017-06716 and 2020-05421 and from NanoLund is gratefully acknowledged. We thank the ISIS Neutron and Muon source (UK) for allocating beamtime on Sans2d (RB1920532). We also would like to acknowledge Professor Joachim Rädler for inspirational discussion.

Appendix A. Supplementary material

Supplementary material related to this article can be found online at https://doi.org/10.1016/j.jcis.2023.12.165.

References

[1] X. Hou, T. Zaks, R. Langer, Y. Dong, Lipid nanoparticles for mRNA delivery, Nat. Rev. Mater. 6 (2021) 1078–1094.
S
[2] A. Akinc, et al., The Onpattro story and the clinical translation of nanomedicines containing nucleic acid-based drugs, Nat. Nanotechnol. 14 (2019) 1084–1087.
[3] L.R. Baden, et al., Efficacy and safety of the mRNA-1273 Sars-CoV-2 vaccine, N. Engl. J. Med. 384 (2021) 403–416, PMID: 33378609.
[4] F.P. Polack, et al., Safety and efficacy of the BNT162b2 mRNA Covid-19 vaccine, N. Engl. J. Med. 383 (2020) 2603–2615, PMID: 33301246.
[5] E. Samaridou, J. Heyes, P. Lutwyche, Lipid nanoparticles for nucleic acid delivery: current perspectives, Adv. Drug Deliv. Rev. 154–155 (2020) 37–63.
[6] K.A. Hajj, K.A. Whitehead, Tools for translation: non-viral materials for therapeutic mRNA delivery, Nat. Rev. Mater. 2 (2017) 17056.
[7] S.C. Semple, S.K. Klimuk, T.O. Harasym, N.D. Santos, S.M. Ansell, K.F. Wong, N. Maurer, H. Stark, P.R. Cullis, M.J. Hope, P. Scherrer, Efficient encapsulation of antisense oligonucleotides in lipid vesicles using ionizable aminolipids: formation of novel small multilamellar vesicle structures, Biochim. Biophys. Acta, Biomembr. 1510 (2001) 152–166.
[8] S.C. Semple, et al., Rational design of cationic lipids for siRNA delivery, Nat. Biotechnol. 28 (2010) 172–176.
[9] J. Heyes, L. Palmer, K. Bremner, I. MacLachlan, Cationic lipid saturation influences intracellular delivery of encapsulated nucleic acids, J. Control. Release 107 (2005) 276–287.
[10] A. Akinc, et al., A combinatorial library of lipid-like materials for delivery of RNAi therapeutics, Nat. Biotechnol. 26 (2008) 561–569.
[11] J.A. Kulkarni, D. Witzigmann, J. Leung, Y.Y.C. Tam, P.R. Cullis, On the role of helper lipids in lipid nanoparticle formulations of siRNA, Nanoscale 11 (2019) 21733–21739.
[12] J.A. Kulkarni, M.M. Darjuan, J.E. Mercer, S. Chen, R. van der Meel, J.L. Thewalt, Y.Y.C. Tam, P.R. Cullis, On the formation and morphology of lipid nanoparticles containing ionizable cationic lipids and siRNA, ACS Nano 12 (2018) 4787–4795, https://doi.org/10.1021/acsnano.8b01516.
[13] J.A. Kulkarni, D. Witzigmann, J. Leung, R. van der Meel, J. Zaifman, M.M. Darjuan, H.M. Grisch-Chan, B. Thöny, Y.Y.C. Tam, P.R. Cullis, Fusion-dependent formation of lipid nanoparticles containing macromolecular payloads, Nanoscale 11 (2019) 9023–9031.
[14] M.H.Y. Cheng, J. Leung, Y. Zhang, C. Strong, G. Basha, A. Momeni, Y. Chen, E. Jan, A. Abdolahzadeh, X. Wang, J.A. Kulkarni, D. Witzigmann, P.R. Cullis, Induction of bleb structures in lipid nanoparticle formulations of mRNA leads to improved transfection potency, Adv. Mater. 35 (31) (2023) 2303370, https://doi.org/10.1002/adma.202303370.
[15] M.Y. Arteta, T. Kjellman, S. Bartesaghi, S. Wallin, X. Wu, A.J. Kvist, A. Dabkowska, N. Székely, A. Radulescu, J. Bergenholtz, L. Lindfors, Successful reprogramming of cellular protein production through mRNA delivered by functionalized lipid nanoparticles, Proc. Natl. Acad. Sci. 115 (2018) E3351–E3360.
[16] F. Sebastiani, et al., Apolipoprotein e binding drives structural and compositional rearrangement of mRNA-containing lipid nanoparticles, ACS Nano 15 (2021) 6709–6722, https://doi.org/10.1021/acsnano.0c10064.
[17] M. Hammel, Y. Fan, A. Sarode, A.E. Byrnes, N. Zang, P. Kou, K. Nagapudi, D. Leung, C.C. Hoogenraad, T. Chen, C.-W. Yen, G.L. Hura, Correlating the structure and gene silencing activity of oligonucleotide-loaded lipid nanoparticles using small-angle X-ray scattering, ACS Nano 17 (2023) 11454–11465, https://doi.org/10.1021/acsnano.3c01186.
[18] H. Yu, A. Angelova, B. Angelov, B. Dyett, L. Matthews, Y. Zhang, M.E. Mohamad, X. Cai, S. Valimehr, C.J. Drummond, J. Zhai, Real-time pH-dependent self-assembly of ionisable lipids from Covid-19 vaccines and in situ nucleic acid complexation, Angew. Chem., Int. Ed. (2023).
[19] K. An, D. Kurek, M. Mahadeo, Y. Zhang, J.L. Thewalt, P.R. Cullis, J.A. Kulkarni, On the influence of nucleic acid backbone modifications on lipid nanoparticle morphology, Langmuir 38 (2022) 14036–14043, https://doi.org/10.1021/acs.langmuir.2c01492.
[20] M. Cárdenas, R.A. Campbell, M.Y. Arteta, M.J. Lawrence, F. Sebastiani, Review of structural design guiding the development of lipid nanoparticles for nucleic acid delivery, Curr. Opin. Colloid Interface Sci. 66 (2023) 101705.
[21] M. Ramezanpour, M.L. Schmidt, I. Bodnariuc, J.A. Kulkarni, S.S.W. Leung, P.R. Cullis, J.L. Thewalt, D.P. Tieleman, Ionizable amino lipid interactions with POPC: implications for lipid nanoparticle function, Nanoscale 11 (2019) 14141–14146.
[22] S. Li, Y. Hu, A. Li, J. Lin, K. Hsieh, Z. Schneiderman, P. Zhang, Y. Zhu, C. Qiu, E. Kokkoli, T.-H. Wang, H.-Q. Mao, Payload distribution and capacity of mRNA lipid nanoparticles, Nat. Commun. 13 (2022) 5561.
[23] M. Mura, B. Humphreys, J. Gilbert, A. Salis, T. Nylander, Cation and buffer specific effects on the DNA-lipid interaction, Colloids Surf. B, Biointerfaces 223 (2023) 113187.
[24] J. Gilbert, I. Ermilova, M. Fornasier, M. Skoda, G. Fragneto, J. Swenson, T. Nylander, On the interactions between RNA and titrateable lipid layers: implications for RNA delivery with lipid nanoparticles, Nanoscale (2024).
[25] Y. Sakurai, T. Hada, H. Harashima, Scalable preparation of poly(ethylene glycol)-grafted siRNA-loaded lipid nanoparticles using a commercially available fluidic

device and tangential flow filtration, J. Biomater. Sci., Polymer Ed. 28 (2017) 1086–1096, https://doi.org/10.1080/09205063.2017.1291297.
[26] H.-W. Liu, Y. Hu, Y. Ren, H. Nam, J.L. Santos, S. Ng, L. Gong, M. Brummet, C.A. Carrington, C.G. Ullman, M.G. Pomper, I. Minn, H.-Q. Mao, Scalable purification of plasmid DNA nanoparticles by tangential flow filtration for systemic delivery, ACS Appl. Mater. Interfaces 13 (2021) 30326–30336, https://doi.org/10.1021/acsami.1c05750.
[27] J. Philipp, et al., pH-dependent structural transitions in cationic ionizable lipid mesophases are critical for lipid nanoparticle function, Proc. Natl. Acad. Sci. 120 (2023) e2310491120, https://doi.org/10.1073/pnas.2310491120.
[28] J. Thrierr, M. Dourlent, M. Leng, A study of polyuridylic acid, J. Mol. Biol. 58 (1971) 815–830.
[29] M.I. Zarudnaya, I.M. Kolomiets, A.L. Potyahaylo, D.M. Hovorun, Structural transitions in poly(A), poly(C), poly(U), and poly(G) and their possible biological roles, J. Biomol. Struct. Dyn. 37 (2019) 2837–2866, https://doi.org/10.1080/07391102.2018.1503972.
[30] M.I. Zarudnaya, Study of conformational transitions in poly(A) by the buffer capacity technique, Mol. Biol. 32 (1998) 417–422.
[31] M.I. Zarudnaya, N.V. Zheltovskii, Electrophoretic analysis of conformational transitions in poly(A) at acidic pH, Mol. Biol. 29 (1995) 611–615.
[32] A.G. Petrovic, P.L. Polavarapu, Structural transitions in polyriboadenylic acid induced by the changes in pH and temperature: vibrational circular dichroism study in solution and film states, J. Phys. Chem. B 109 (2005) 23698–23705, https://doi.org/10.1021/jp054280m.
[33] P.C. Bevilacqua, L.E. Ritchey, Z. Su, S.M. Assmann, Genome-wide analysis of RNA secondary structure, Annu. Rev. Genet. 50 (2016) 235–266, https://doi.org/10.1146/annurev-genet-120215-035034.
[34] M. Egli, A. Flavell, A.M. Pyle, W.D. Wilson, S.I. Haq, B. Luisi, J. Fisher, C. Laughton, S. Allen, J. Engels, G.M. Blackburn, M.J. Gait, D. Loakes, D.M. Williams, Nucleic Acids in Chemistry and Biology, 3rd ed., The Royal Society of Chemistry, 2006, pp. 1–142.
[35] T. Sych, J. Schlegel, H.M.G. Barriga, M. Ojansivu, L. Hanke, F. Weber, R.B. Bostancioglu, K. Ezzat, H. Stangl, B. Plochberger, J. Laurencikiene, S.E. Andaloussi, D. Fürth, M.M. Stevens, E. Sezgin, High-throughput measurement of the content and properties of nano-sized bioparticles with single-particle profiler, Nat. Biotechnol. (2023).
[36] L.J. Jones, S.T. Yue, C.-Y. Cheung, V.L. Singer, RNA quantitation by fluorescence-based solution assay: RiboGreen reagent characterization, Anal. Biochem. 265 (1998) 368–374.
[37] A.B. Jensen, T.E.K. Christensen, C. Weninger, H. Birkedal, Very large-scale diffraction investigations enabled by a matrix-multiplication facilitated radial and azimuthal integration algorithm: MatFRAIA, J. Synchrotron Radiat. 29 (2022) 1420–1428.
[38] O. Arnold, et al., Mantid—data analysis and visualization package for neutron scattering and μ SR experiments, Nucl. Instrum. Methods Phys. Res., Sect. A, Accel. Spectrom. Detect. Assoc. Equip. 764 (2014) 156–166.